The effect of increasing Si content in the absorber layers ($CrAlSiN_x$ /$CrAlSiO_yN_x$) of solar selective absorbers upon their selectivity and thermal stability

A. AL-Rjoub[a], L. Rebouta[a,1], P. Costa[a], N. F. Cunha[a], S. Lanceros-Mendez[b,c,d], N.P. Barradas[e], E. Alves[f]

a Centre of Physics, University of Minho, Campus de Azurém, 4800-058 Guimarães, Portugal
b BCMaterials, Basque Center for Materials, Applications and Nanostructures, UPV/EHU Science Park, 48940 Leioa, Spain
c IKERBASQUE, Basque Foundation for Science, 48013 Bilbao, Spain
d Centre of Physics, University of Minho, Campus de Gualtar, 4710-057 Braga, Portugal
e Centre for Nuclear Sciences and Technologies, IST, University of Lisbon, Bobadela, Portugal
f Institute for Plasmas and Nuclear Fusion, IST, University of Lisbon, Lisbon, Portugal

Abstract

In this work, the effect of increasing Si content in the absorber layers ($CrAlSiN_x$ /$CrAlSiO_yN_x$) of solar selective absorbers upon their selectivity and thermal stability are studied. The two optical stacks presented consist of four magnetron sputtered layers on stainless steel substrates. In both cases, tungsten is used as back-reflector, $CrAlSi_xN$/$CrAlSiO_yN_x$ as absorber layers with different Si/(Cr+Al+Si) atomic ratio (0.15 and 0.30, respectively) and finally the $SiAlO_x$ antireflection layer. The structures were theoretically designed by SCOUT software depended on experimental transmittance (T) and reflectance (R) of thin single layers deposited on glass substrates. It is observed that optical stack coatings with higher silicon content show better selectivity values, high solar absorptance, α= 95.9%, and low emissivity, ε= 9.7 % (calculated for 400 ºC), with higher thermal stability at 600 ºC in vacuum, for 650 h. Additionally, with the annealing at 600 ºC an increase of surface roughness was found, which was smaller for sample with higher Si content.

Keywords: optical properties, selective absorption, emissivity, solar absorptance

1. Introduction

Selective solar thermal absorber coatings are divided into two main groups, the first being based on Cermets as the studied presented in [1-4] and the second are the metal nitrides and oxynitrides based on structures like the ones presented in [5-7]. Cermets allow to obtain efficient absorbers by changing their metal volume fraction to optimize their absorptance and emission [8].

On the other hand, transition metal nitrides and oxynitrides based on structure are characterized by a good diffusion barrier, high resistance of oxidation and thermal stability [6,7, 9-14]. Several transition metals were already used, such as, Ti, Cr,W, Nb, Zr and Al [6,7, 9-11, 14-18].

[1] Corresponding author – e-mail address: rebouta@fisica.uminho.pt (L. Rebouta)

However, high selectivity of such coatings is vital condition to have high efficient thermal absorber stacks. Selectivity means that any design should show a high absorptance (α) at the solar radiation region and a low thermal emittance in the IR region.

In previous studies [9,12], a design of selective solar thermal absorber stacks based on nitride/oxynitride absorber layers structure ($W/CrAlSiN_x/CrAlSiO_yN_x/SiAlO_x$) [9] was presented. The best results showed simultaneously a high solar absorbance α = 95 % and low emissivity ε= 12 % (calculated at 400 ºC) with good thermal stability at 400 ºC in air and at 600 ºC in vacuum, respectively. The current work studies the effect of varying the Si contents of the nitride and the oxynitride upon the thermal stability and absorber selectivity.

2. Experimental

DC magnetron sputtering have been used for all coating with Ar as sputtering gas, working pressure of 0.37 Pa, density of current of 6.4 mA/cm^2, pulsed bias of -60 V, f =90 kHz, initial chamber pressure 2×10^{-4} Pa and room temperature. In the case of tungsten, a density of current 12.7 mA/cm^2 was used. All substrates were carefully cleaned in acetone by ultra sound and under vacuum, a plasma etching was performed. A (99.99%) tungsten target was used for the tungsten layer deposition. Small Si disks were uniformly distributed on a 10 cm diameter Cr70% Al 30% target erosion zone to change the Si content in coatings. Two designs with different Si content are presented in this work; D1 with 5 Si pellets and D2 with 11 Si pellets. The antireflection $SiAlO_x$ layer was deposited using Si80 Al20 at% target and oxygen reactive gas.

For both designs, and in order to obtain the optical properties, single $CrAlSiN_x$ and $CrAlSiO_yN_x$ layers were deposited on glass substrates with different Si content (5 and 11 silicon discs) and different nitrogen and oxygen partial pressures for 1 min. This allowed to select those with adequate optical properties, and the used single layers, $CrAlSiN_x$ and $CrAlSiO_yN_x$, prepared with 11 and 5 Si pellets, are identified as N-11Si, ON-11Si, N-5Si and ON-5Si, respectively. For nitrides and oxynitrides layers, partial pressures of nitrogen (P_N= 0.05 Pa) and oxygen and nitrogen (P_{ON}= 0.07 Pa), respectively, were used as reactive gases.

Transmittance (T) and the reflectance (R) of those layers, in 0.25 – 2.5 μm wavelength range, were performed with a Shimadzu PC3100 spectrophotometer. An Al reference mirror was used to correct the reflectance curves. Those measurements were used to calculate the optical constants (n and k) and thicknesses of designed layers as described in previous studies [9,12]. Selective absorber stacks were designed based on the data obtained from single layers, and deposited on Si and stainless-steel substrates with parameters presented in Table I.

Table I: D1 and D2 deposition parameters.

Sample	Layer	Target	Deposition time (min)	Reactive gas and partial pressure (Pa)	Thickness (nm)
D1	W	W	2:00	-	120
	$CrAlSiN_x$ (N-5Si)	CrAl+ 5 Si	1: 27	N_2 0.05	63
	$CrAlSiO_yN_x$ (ON-5Si)	CrAl+ 5 Si	0:23	N_2/O_2 (85%/15%) 0.07	16
	$SiAlO_x$	SiAl	1:29	O_2 0.06	77
D2	W	W	2:00	-	120
	$CrAlSiN_x$ (N-11Si)	CrAl+11 Si	2:20	N_2 0.05	59
	$CrAlSiO_yN_x$ (ON-11Si)	CrAl+11Si	1:26	N_2/O_2 (85%/15%) 0.07	35
	$SiAlO_x$	SiAl	1: 19	O_2 0.06	68

For the thermal stability tests, the absorber stacks were annealed in air and in vacuum at 450 ºC and 600 ºC, respectively for 650 h. in the case of experiments under vacuum, the initial pressure of the furnace was 5.0 mPa. The normal solar absorptance (α_s) and normal thermal emittance were calculated in the same way presented in previous works [9]

X-ray diffraction XRD in glancing incident angle mode was applied to study the structure and the oxidation resistance of the samples using a Bruker AXS Discover D8 apparatus operating with Cu Kα radiation. All measurements were performed the incidence angle of α = 3º. A Nano SEM–FEI Nova 200(FEG/SEM) microscope was used for Scanning electron microscopy (SEM) to determine the coatings thickness, morphology and chemical composition, which was assessed by means of EDS analyses with an acceleration voltage of 7 keV. Film topography and surface roughness were studied using Atomic Force Microscope (Dimension Icon- Bruker) under scan adjust mode.

The CTN/IST Van de Graaff accelerator was used to perform the Rutherford Backscattering (RBS) measurements with 2 MeV $^4He^+$ beam and detectors at 165º to the beam direction and IBA Data Furnace NDF software was also used to analyse the data [19].

3. Results and discussion

3.1 Optical properties of single layers

Fig. 1 shows the transmittance (T), reflectance (R), refractive index (n) and extinction coefficient (k) of the individual layers used in both designs D1 and D2, as a function of wavelength in the range of 300 – 2500 nm. The n and k curves were simulated from the modeling of the experimental transmittance and reflectance spectra. The algorithm used by SCOUT software also allows the calculation of the thicknesses simultaneously with T and R modeling [20] and thus, estimate the deposition rate. The thin layers N-5Si, N-11Si, ON-5Si and ON-11Si, whose results are shown in Fig. 1, have thicknesses of 42 nm, 31 nm, 38 nm and 36 nm, respectively. The deposition time was the same for all, and this shows that when the number of Si inserts was increased, the deposition rate decreased being the effect higher in case of nitrides. Increasing Si content in the $CrAlSiN_x$ and $CrAlSiO_yN_x$ layers leads to a higher transparency. The refractive index (n) of N-11Si is slightly higher than the one of N-5Si, but the extinction coefficient of N-11Si is lower than the one of N-5Si. For oxynitrides, ON-11Si shows lower n and k when compared with those prepared with 5 Si discs. This means that increasing Si content in the films and using the same partial pressure of reactive gases, leads to more transparent layers, due to the formation of Si nitride and Si oxynitride, which are transparent. The increase of Si content implies a decrease of Cr content, which leads to non-transparent nitrides. The presence of Si nitride and oxynitride will improve the thermal and chemical stability but can impoverish the optical properties. Thus, the increase of the Si content should be limited in order to maintain the optical properties in the required range.

The interference effect can be used to optimize the solar absorptance. With three layers it is possible to have, in the reflectance spectra, two minima in the wavelength range of solar radiation. The refractive indices and thicknesses of the bilayer structure should be selected to get a phase cancellation position at wavelengths around 0.5 μm and 1.3 μm, which decreases the reflectance of the solar radiation and enhancing its absorptance [21].

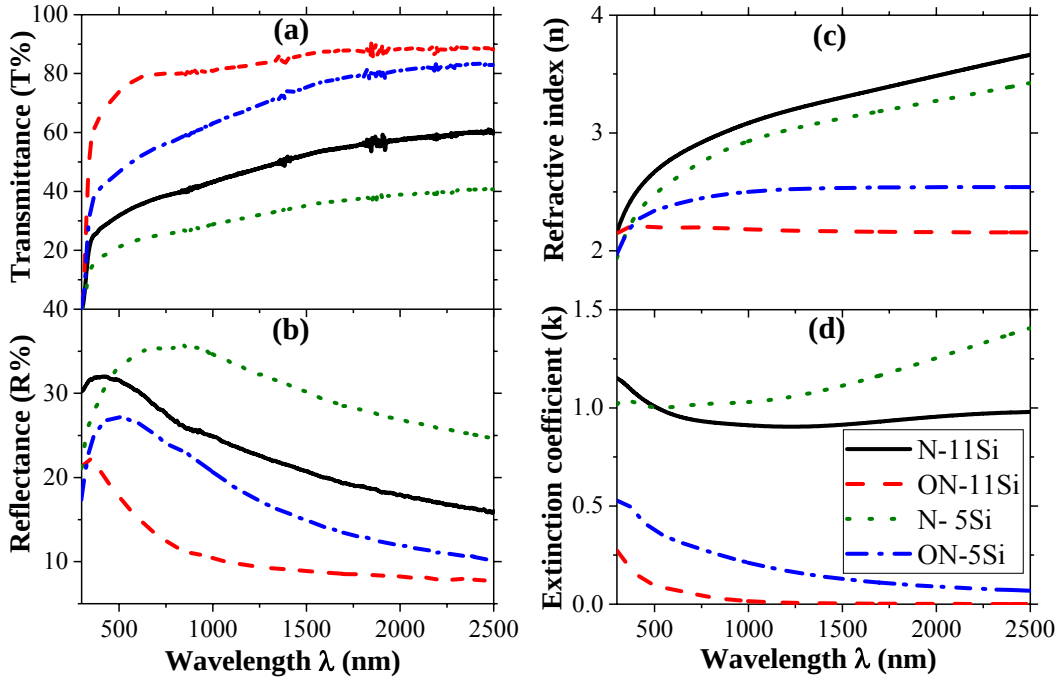

Fig. 1: (a)Transmittance (T), (b) Reflectance (R), (c) Refractive index (n) and (d) extinction coefficient (k) of $CrAlSiN_x$ and $CrAlSiO_yN_x$ as a function of wavelength (λ).

In both designs, tungsten was used as back-reflector layer and $SiAlO_x$ as antireflection layer. These two layers were studied in detail in the previous works [9,12,18]. Tungsten shows a high reflectance in the IR region of radiation (R% = 94.6 at λ ~ 2.5 µm), whereas the antireflection layer ($SiAlO_x$) is transparent and has a very low extinction coefficient and a refractive index around 1.50. This layer is a good barrier diffusion, protecting the other layers.

3.2 Chemical composition of the single layers

The chemical composition of thick layers like those used in the optical stacks are presented in Table II. An average of two EDS measurements randomly performed for two points on the surface of each sample was calculated. When the number of Si discs decreased from 11 to 5, a 25 % decrease in the (Al+Si)/Cr elemental ratio in nitride and oxynitride samples is observed, and the Si/(Si+Al+Cr) atomic ratio changed from 0.3 to 0.15. This change in the elemental content ratio is enough to obtain different optical properties, as already described in the previous section. The Si discs were placed on the CrAl target, which means that the increase of Si implies a reduction of Al and Cr, as shown in table II. AlN is also transparent, but the (Al+Si)/Cr elemental ratio can play an important role in other properties of the films. The oxygen and the nitrogen reactive gases partial pressures have a big influence on the structure,

chemical and thermal stability of the layers. Stoichiometric films are more thermally and chemically stable, but usually they do not have the adequate optical properties and it is necessary to deposit sub-stoichiometric films to obtain those optical properties.

Table II: EDS chemical composition and thickness of N-11Si, ON-11Si, N-5Si and ON-5Si thick layers.

Layer	N at%	O at%	Al at%	Si at%	Cr at%	Si/(Si+Al+Cr)	N+O/(Al+Si+Cr)	(Al+Si)/Cr	Thickness (µm)
N-5Si	23	6	30	11	30	0.15	0.4	1.5	1.3
N-11Si	26	5	26	20	23	0.29	0.5	2.0	0.9
ON-5Si	27	18	25	8	22	0.145	0.8	1.5	1.4
ON-11Si	30	11	22	18	19	0.305	0.7	2.0	1.1

3.3 Structure of the single layers

The absorption layers used in both absorber stacks, the nitrides and oxynitrides layers, were analyzed by XRD, and the corresponding diffractograms are represented in Fig. 2. Some layers show broad peaks, which is typical for materials with small grain size, and other layers amorphous. Moreover, cross section SEM micrographs (Fig. 3) agree with the XRD analysis showing a compact featureless morphology.

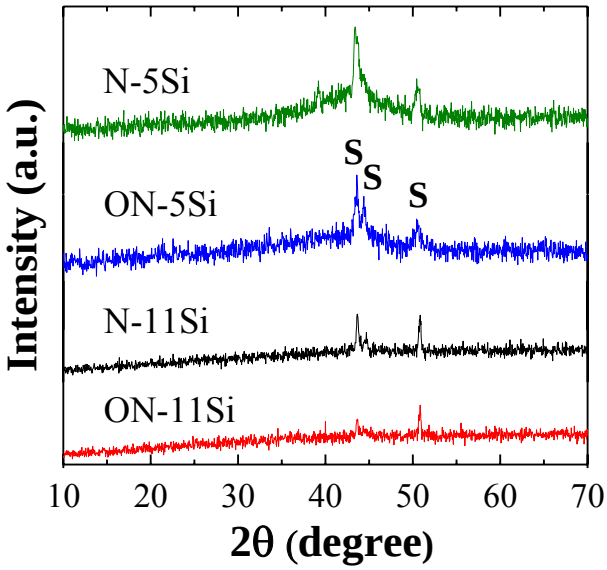

Fig. 2: XRD of the single layers. (S related to stainless steel structure.)

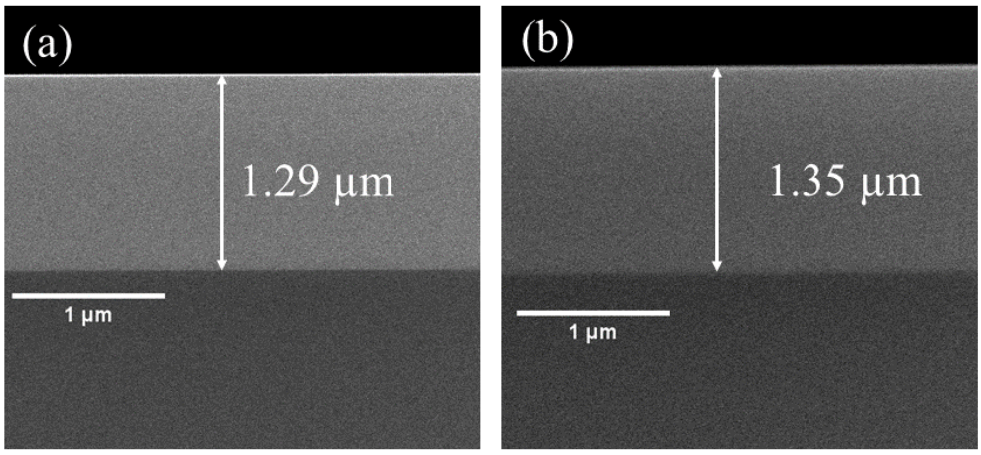

Fig. 3: SEM cross-section micrographs of (a) N-5Si and (b) ON-5Si samples.

3.4 Design of the multilayer

The multilayers absorber stacks D1 and D2 were designed and optimized based on the data obtained from transmittance and reflectance of thin single layers with SCOUT software, with some deposition parameters described in table I. The thicknesses of each layer, the simulated and as deposited reflectance with calculated absorptance (α) of both stacks are shown in Fig. 4. The total simulated thickness of D1 and D2 are 276 nm and 282 nm, respectively. Both multilayers experimental designs show good agreement with the simulated ones. The final designs show simultaneously high average solar absorbance (α_{D1}= 94.6 % and α_{D2}= 95.9 %) and low emissivity (ε_{D1}= 11.1 % and ε_{D2}= 9.7 %, calculated for 400 ºC). Sample D2 shows better selectivity (α/ε), mainly because its single layers have more adequate optical constants, which is confirmed by the minimums at about 600 nm and 1300 nm due to the interference effect

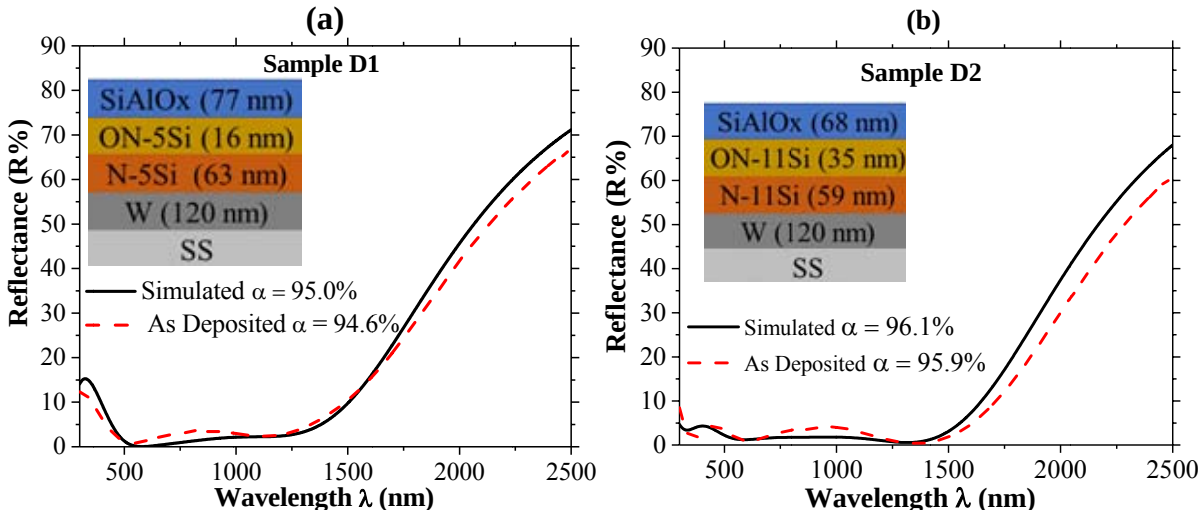

Fig. 4: Schematic diagram of the simulated multilayer as obtained by SCOUT with simulated and experimental reflectance curves of the absorber design (a) D1 and (b) D2.

Furthermore, Fig. 5 shows SEM cross-section micrographs of the two samples deposited on Si substrates. Only W layer shows the columnar growth morphology and the remaining layers seem to be amorphous that agrees with XRD analysis of the similar thick layers presented in section 3.3. The total thickness is similar to those in the simulated design. The change in composition from nitride to oxynitride is mainly the increase of light elements, and this is not enough to distinguish the nitride from the oxynitride in the SEM micrographs.

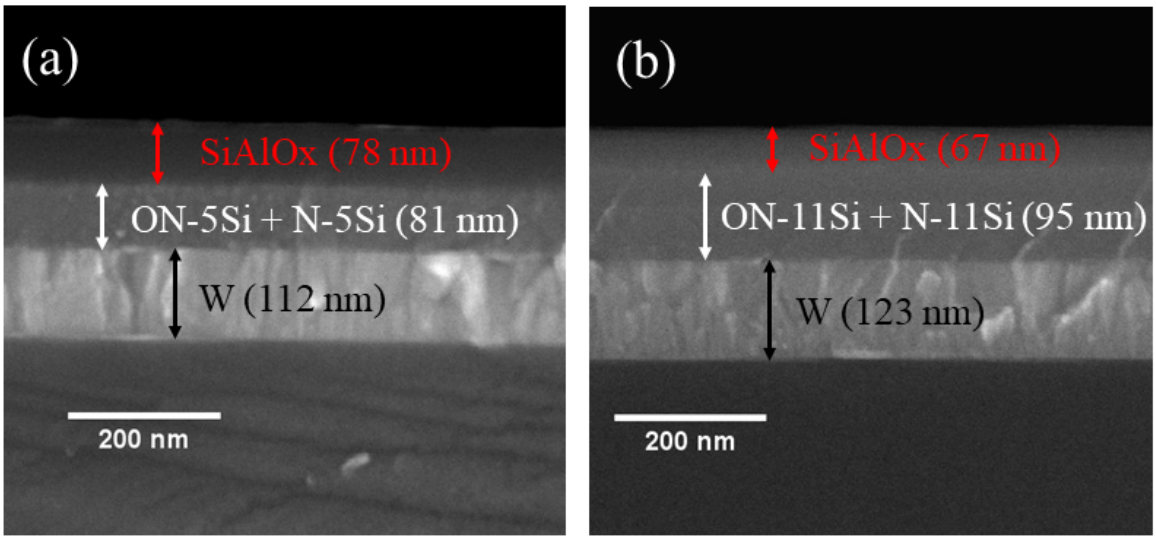

Fig. 5: Cross-sectional SEM images of samples D1 and D2.

3.5 Thermal stability

Thermal stability and good resistance to oxidation is a core need to selective thermal absorbers for long lifetime use. The performance of optical stacks was evaluated with to annealing tests in air at 450 ºC and in vacuum at 600 ºC for 650 h, and the solar absorptance (α) and the emittance (ε) were used as control parameters. The results are presented in Fig.6, where are represented the reflectance curves of the as deposited samples and after 650 h of air and vacuum annealing. As shown in Fig.6a and Fig. 6b, both samples D1 and D2 show excellent thermal stability after annealing in air with almost no changes on the reflectance curves and absorbance (α), which confirm that both stacks are adequate for this high temperature (450 ºC). On the other hand, the stack with higher Si content (D2) shows much better thermal stability than the D1 one after vacuum annealing at 600 ºC. The changes in the reflectance curve of sample D1 (Fig. 6a) resulted in a decrease of the absorbance (α) of 1.1%. In all cases, the emittance (ε) is improved after annealing in air and in vacuum, which confirms that the tungsten reflection layer is well protected by the other layers, showing good thermal stability against oxidation. The decrease of the

emissivity with annealing was already reported and can be due to a W phase transformation during annealing [22,23].

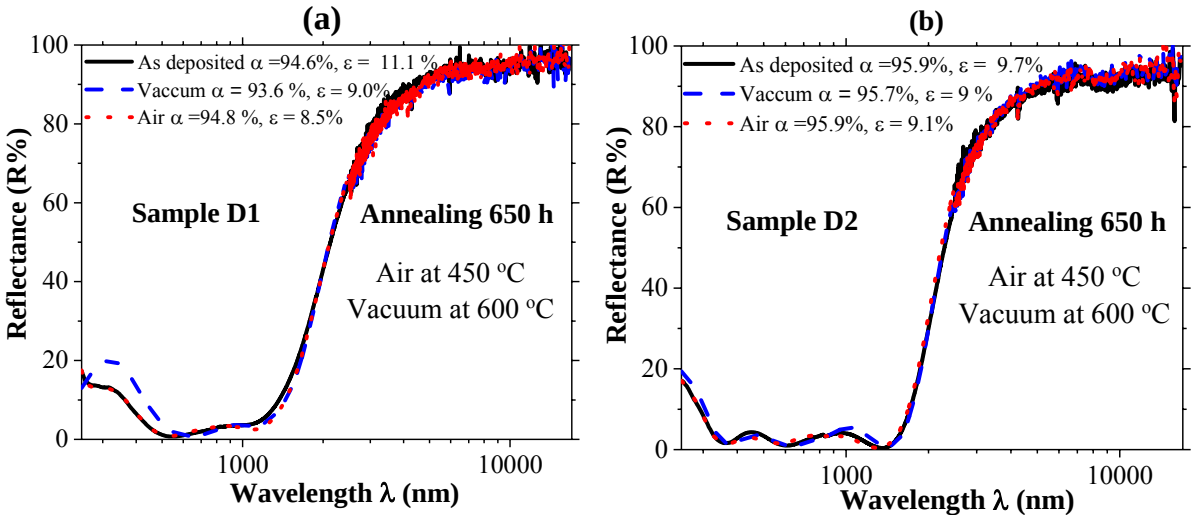

Fig. 6: Reflectance of as deposited and after air and vacuum thermal annealed samples (the thermal emittance (ε) was calculated for 400 ºC).

Further tests upon the thermal stability and the evaluation of elemental diffusion were performed by RBS, where the elemental depth profiles of each absorber were studied. The RBS spectra of the as deposited and after vacuum and air annealed samples for 650 h are shown in Fig. 7a and b. For better understanding, the front edges of the different elements, if located at surface sample, are indicated in the figures. From the spectra it is clearly observed that W and absorption layers (AL) of sample D2 (Fig. 7b) are thicker than those of sample D1 (Fig. 7a), confirming what is shown in Fig. 5. Small differences between the spectra of the as deposited and after annealing samples were obtained and the analysis emphasized that differences in the region of channel numbers 560-580 are related with depth profile of W element and corresponds to a tail elongation of the back side of W layer, as also confirmed in the previous studies [9,12]. As a result, small amount of tungsten diffused towards the stainless-steel substrate, but the general evaluation shows that no other significant changes are present. However, tungsten diffusion towards the substrate can be easily solved by adding a barrier layer, as studied in the previous work [22]. The small changes seen after the vacuum annealing, shown in Fig. 6, should be related with diffusion processes other that are not related with the tungsten diffusion towards the substrate, which cannot be seen in reflectance curves. From Fig. 7 cannot be excluded the small widening of the interface between W layer and the absorption layer and other diffusion processes are not clearly seen in Fig. 7, but in sample D2 (Fig. 6 b) are certainly lower than in sample D1 (Fig. 6 a).

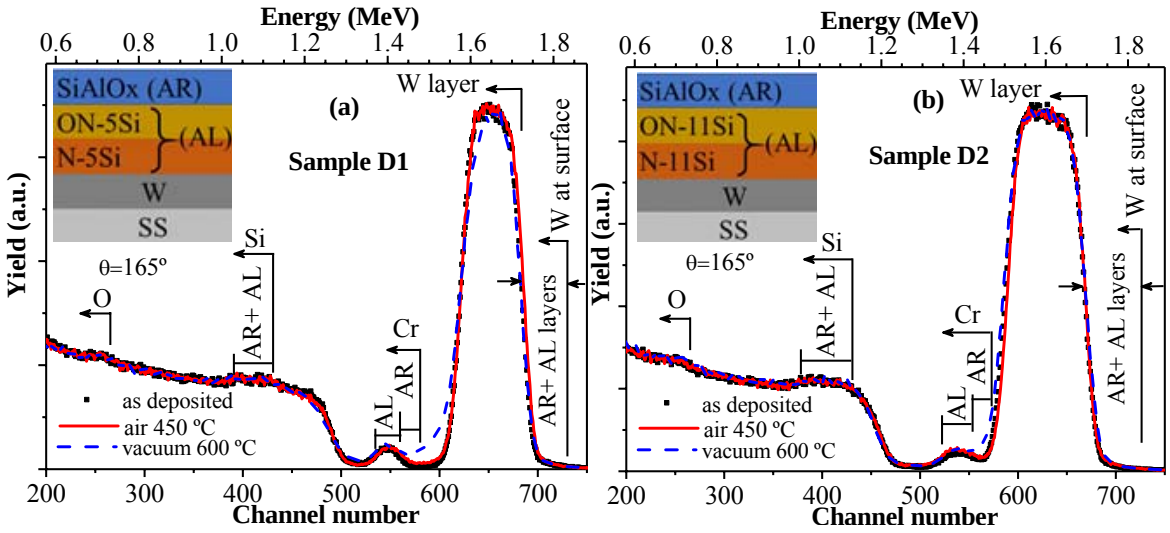

Fig. 7: The spectra of RBS of the samples D1 and D2 as deposited and after air and vacuum annealing for 650 h.

The two samples were analyzed by XRD to have more information about any further structural changes after air and vacuum annealing. In Fig. 8 are represented the diffractograms of samples before and after annealing, and all samples showed no significant changes after the annealing except for small differences in the intensity of W peaks. As already shown with reflectance curves (Fig. 6), this behavior is in accordance with good resistance against oxidation and thermal stability. The peak located at 36º in Fig.8a, is addressed to W β-phase, which contributes for higher emittance of the as deposited D1 sample. The β-W phase is favored when the base pressure before the deposition of the W layer is not good enough. The β-W phase has higher electrical resistivity than α-W phase and its presence contributes for the resistivity increase of the W layer and consequent emittance increase [24].

Moreover, the tungsten layer in sample D2 does not have any β-phase structure, which means it contributed for improving of the emittance of the whole stack. Annealing induces the transformation from tungsten β- to α- phase together with a decrease of the emittance, as shown in Fig. 8 and Fig. 6. The peak at ~36º in Fig. 6a has becomes thinner after the annealing. A transformation from tungsten β- to α- phase was also reported by other authors [23] with a small increase in the reflectance for wavelengths higher than 2 μm. In the case of sample D2, the contamination of the W layer was smaller, as the presence of β-W phase is not evident, but the decrease of the emittance with the annealing suggests an improvement of the resistivity of the W layer, which is related to the reflectance in the IR wavelength range. In Fig.8 are also included the grain sizes of tungsten layer, in as deposited state and after annealing, which were calculated from the full width at half maximum (FWHM) of (110) tungsten peak and using the Scherrer equation [25]. The grain size revealed a slight increase with the annealing in vacuum at 600 ºC (from ~17

nm to ~26 nm), but no significant changes were seen after the annealing in air at 450 ºC. This grain growth is related with recrystallization associated with a decrease of grain boundary area, but can also be related with the mentioned phase transformation, which can happen at 600 ºC, when the oxygen concentration is low (1-2 at.% O) [26].

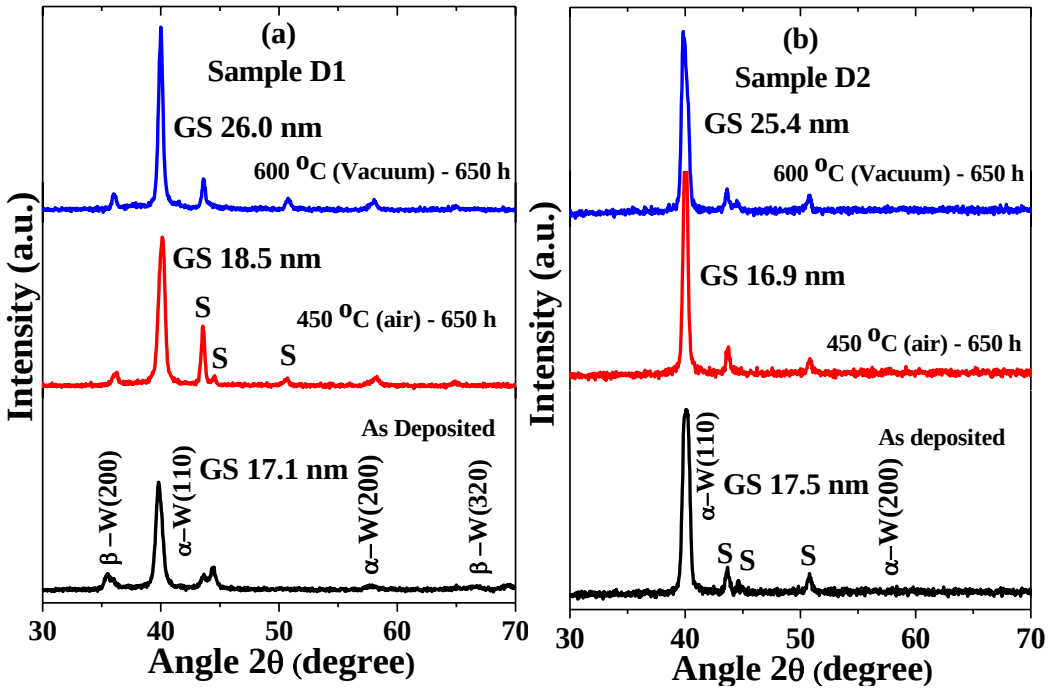

Fig. 8: XRD diffractograms of as deposited samples D1 and D2 in the as deposited state and after air and vacuum annealing.

Surface roughness of samples D1 and D2 were studied by AFM, one in as deposited state and a second annealed in vacuum at 600 ºC. The surface roughness R_a was averaged from two 5x5 μm^2 scans, and the AFM micrographs of the as-deposited and annealed films are presented in Fig. 9. Some scratches can be seen, which are due to the mechanical surface polishing prior the deposition. The surface morphology of as deposited samples (Fig. 9a and Fig. 9c) indicates featureless grain growth indicating no clear grain formation, which is in agreement with the amorphous structure. With the annealing a small spike formation was found (Fig. 9b and Fig. 9d) and the surface roughness revealed a small increase, changing from R_a=2.2 nm for the as deposited state to 5.7 nm after the annealing in vacuum for sample D1, and from R_a=2.1 nm to 4.9 nm for sample D2. The difference is not significant, but the sampleD2, with higher Si content is also the sample with better performance when subjected to thermal annealing. The surface roughness of as deposited samples is similar to other selective absorber coating based on AlSiOx:W cermets [27]. However, the surface roughness of those cermets after annealing was lower, but the time annealing time was also much lower.

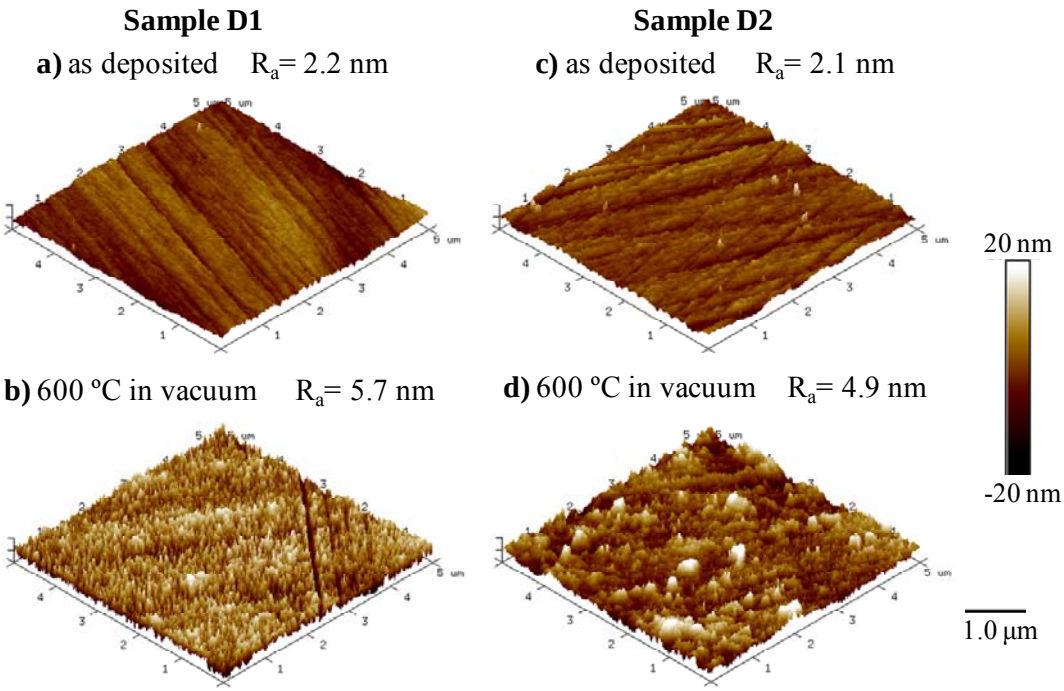

Fig. 9: Surface roughness imaged by AFM (5x5 μm^2) of sample D1: a) as deposited coating; b) after annealing at 600 ºC in vacuum and of sample D2: a) as deposited coating; b) after annealing at 600 ºC in vacuum.

As a summary, the sample with higher Si content (D2) revealed a better thermal stability with annealing in vacuum, which can be mainly related with atomic diffusion, because the annealing was performed in vacuum, where the oxidation processes are minimized. The diffusion barrier properties were improved with the increase of Si content. The films are sub-stoichiometric with (N+O)/(Al+Si+Cr) atomic ratio of about 0.43-0.45 for nitrides and 0.7 -0.8 for oxynitride. Thus, those layers (mainly for nitrides) contain some of Cr atoms in metallic oxidation state, which favors the diffusion, and Si has apparently an important role in the improvement of the barrier properties. With the annealing at 600 ºC, an increase of the surface roughness was found, being smaller for sample with higher Si content.

4. Conclusions

Two designs of solar selective absorber for high temperature applications were presented. The designs consist on multilayer based on a structure of four layers ($W/CrAlSiN_x$ /$CrAlSiO_yN_x$ /$SiAlO_x$), with different Si content (5 and 11 silicon discs on CrAl target), which correspond to a Si/(Si+Al+Cr) atomic ratio of 0.15 and 0.3, respectively. Thick single layers of

$CrAlSiN_x$ and $CrAlSiO_yN_x$ similar to those used in both designs were used to study the structural, optical and chemical properties. Using the same partial pressure of reactive gases, these layers have lower extinction coefficient and become more transparent with increasing silicon content, showing that, the optical constants n and k are sensitive to these changes. The elemental ratio (Al+Si)/Cr decreased by 25 % in nitride and oxynitride samples when the number of Si discs decreased from 11 to 5 and all these layers are amorphous, as confirmed be XRD analysis. Based on the data from these single layers, the tandems were simulated by the SCOUT software and then the stacks were deposited. A small improvement was seen with the increase of Si content (using 5, 9 [9] and 11 Si discs on CrAl target), and the experimental designs of higher silicon content show better selectivity values, high solar absorptance, α=95.9%, and low emissivity, ε= 9.7 % (calculated for 400 ºC), together with higher thermal stability at 600 ºC, in vacuum, for 650 h. Generally, thermal emissivity revealed a small improvement with the thermal annealing, which is related with the tungsten grain size increase and transformation from tungsten β- to α- phase, but also shows that the W back reflector layer is well protected by the outermost layers. The RBS recorded a small amount of tungsten diffused from the back-reflector layer towards the stainless-steel substrate in both designs, which can be avoided by adding a barrier layer. Moreover, after vacuum annealing at 600 ºC, an increase of surface roughness was found, being slightly smaller for sample with higher Si content.. Finally, the $CrAlSiN_x$ /$CrAlSiO_yN_x$ and $SiAlO_x$ layers are amorphous and the tungsten layer is polycrystalline with (110) orientation as confirmed by XRD.

ACKNOWLEDGMENTS

The authors acknowledge the support of FCT in the framework of the Strategic Funding UID/FIS/04650/2013 and the financial support of FCT, POCI and PORL operational programs through the project POCI-01-0145-FEDER-016907 (PTDC/CTM-ENE/2892/2014), co-financed by European community fund FEDER.

References

[1] E. Sani, L. Mercatelli, P. Sansoni, L. Silvestroni, D. Sciti, Spectrally selective ultra-high temperature ceramic absorbers for high-temperature solar plants, J. Renew. Sustain. Energy. 4, 03310 (2012).

[2] C. Gremion, C. Seassal, E. Drouard, A. Gerthoffer, N. Pelissier, C. Ducros, Design , properties and degradation mechanisms of Pt-Al_2O_3 multilayer coating for high temperature solar thermal applications, Surf. Coat. Technol. 284 (2015) 31–37.

[3] H. Wang, H. Alshehri, H. Su, L. Wang, fabrication and optical characterizations of large-area lithography- free ultrathin multilayer selective solar coatings with excellent thermal stability in air, Sol. Energy Mater. Sol. Cells. 174 (2018) 445–452.
[4] A. Rodríguez-palomo, E. Céspedes, D. Hernández-pinilla, C. Prieto, High-temperature air-stable solar selective coating based on $MoSi_2$ – Si_3N_4 composite, Sol. Energy Mater. Sol. Cells. 174 (2018) 50–55.
[5] I. Heras, E. Guillén, F. Lungwitz, G. Rincón-llorente, F. Munnik, E. Schumann, I. Azkona, Design of high-temperature solar-selective coatings based on aluminium titanium oxynitrides Al y $Ti_{1-y}(O_x N_{1-x})$. Part 1□: Advanced microstructural characterization and optical simulation, Sol. Energy Mater. Sol. Cells. 176 (2018) 81–92.
[6] P. Song, Y. Wu, L. Wang, Y. Sun, Y. Ning, Y. Zhang, B. Dai, E. Tomasella, A. Bousquet, C. Wang, The investigation of thermal stability of Al/NbMoN/NbMoON/SiO2solar selective absorbing coating, Sol. Energy Mater. Sol. Cells. 171 (2017) 253–257.
[7] J. Meng, X. Liu, Z. Fu, K. Zhang, Optical design of $Cu/Zr_{0.2}AlN_{0.8}/ZrN/AlN/ZrN/AlN/Al_{34}O_{62}N_4$ solar selective absorbing coatings, Sol. Energy. 146 (2017) 430–435.
[8] Q. Zhang, D.R. Mills, Q. Zhang, D.R. Mills, Very low-emittance solar selective surfaces using new film structures, J. Appl. Phys. 72, 3013 (1992).
[9] A. AL-Rjoub, L. Rebouta, P. Costa, N.P. Barradas, E. Alves, P.J. Ferreira, K. Abderra, A. Matilainen, K. Pischow, A design of selective solar absorber for high temperature applications, Sol. Energy. 172 (2018) 177–183.
[10] J. Feng, S. Zhang, X. Liu, H. Yu, H. Ding, Y. Tian, J. Ouyang, Solar Selective Absorbing Coatings TiN/TiSiN/SiN Prepared on Stainless Steel Substrates, Vacuum. 121 (2015) 135–141.
[11] H.D. Liu, T.R. Fu, M.H. Duan, Q. Wan, Y.M. Chen, D.J. Fu, F. Ren, Q.Y. Li, X.D. Cheng, B. Yang, X.J. Hu, Structure and thermal stability of spectrally selective absorber based on AlCrON coating for solar-thermal conversion applications, Sol. Energy Mater. Sol. Cells. 157 (2016) 108–116.
[12] A. AL-Rjoub, P. Costa, L. Rebouta, I. Bogdanovi, K. Arstila, N.P. Barradas, A study of solar thermal absorber stack based on CrAlSiNx/ CrAlSiNx/Oy structure by ion beams, Nucl. Inst, Methods Phys. Res. B. (2018).
[13] C. Zou, L. Huang, J. Wang, S. Xue, Effects of antireflection layers on the optical and thermal stability properties of a spectrally selective CrAlN – CrAlON based tandem absorber, Sol. Energy Mater. Sol. Cells. 137 (2015) 243–252.
[14] Y. Wu, W. Zheng, L. Lin, Y. Qu, F. Lai, Colored solar selective absorbing coatings with metal Ti and dielectric AlN multilayer structure, Sol. Energy Mater. Sol. Cells. 115 (2013) 145–150.
[15] L. Hao, S. Wang, L. Jiang, X. Liu, H. Li, Z. Li, Preparation and thermal stability on non-vacuum high temperature solar selective absorbing coatings, Chinese Sci. Bull. 54 (2009) 1451–1454.
[16] T.K. Tsai, Y.H. Li, J.S. Fang, Spectral properties and thermal stability of CrN/CrON/ Al_2O_3 spectrally selective coating, Thin Solid Films. 615 (2016) 91–96.
[17] X. Wang, T. Luo, Q. Li, X. Cheng, K. Li, High performance aperiodic metal-dielectric multilayer stacks for solar energy thermal conversion, Sol. Energy Mater. Sol. Cells. 191 (2019) 372–380.
[18] A. AL-Rjoub, L. Rebouta, P. Costa, L.G. Vieira, Multi-layer solar selective absorber

coatings based on W/WSiAlNx/WSiAlOyNx /SiAlOx for high temperature applications, Sol. Energy Mater. Sol. Cells. 186 (2018) 300–308.
[19] N.P. Barradas, C. Jeynes, Advanced physics and algorithms in the IBA DataFurnace, Nucl. Instruments Methods Phys. Res. B. 266 (2008) 1875–1879.
[20] W. Theiβ, Optical properties of porous silicon, Surf. Sci. Rep. 29 (1997) 91–192.
[21] Y. Yin, R.E. Collins, Optimization and analysis of solar selective surfaces with continuous and multilayer profiles, J. Appl. Physiscs. 77, 6485 (1995).
[22] A. AL-Rjoub, L. Rebouta, P. Costa, L.G. Vieira, T.M.R. Miranda, N.P. Barradas, E. Alves, CrAlSiN barrier layer to improve the thermal stability of W/CrAlSiNx/CrAlSiOyNx/SiAlOx solar thermal absorber, Sol. Energy Mater. Sol. Cells. 191 (2019) 235–242.
[23] A. Antonaia, A. Castaldo, M.L. Addonizio, S. Esposito, Stability of W-Al2O3 cermet based solar coating for receiver tube operating at high temperature, Sol. Energy Mater. Sol. Cells. 94 (2010) 1604–1611.
[24] G.S. Chen, L.C. Yang, H.S. Tian, C.S. Hsu, Evaluating substrate bias on the phase-forming behavior of tungsten thin films deposited by diode and ionized magnetron sputtering, Thin Solid Films. 484 (2005) 83–89.
[25] P. Scherrer, Bestimmung der Größe und der inneren Struktur von Kolloidteilchen mittels Röntgenstrahlen, Nachrichten von Der Gesellschaft Der Wissenschaften Zu Göttingen, Math. Klasse. 26 (1918) 98–100.
[26] M.J. O'Keefe, J.T. Grant, Phase transformation of sputter deposited tungsten thin films with A-15 structure, J. Appl. Phys. 79 (1996) 9134–9141.
[27] D. Dias, L. Rebouta, P. Costa, A. AL-Rjoub, M. Benelmeki, C.J. Tavares, N.P. Barradas, E. Alves, P. Santilli, K. Pischow, Optical and structural analysis of solar selective absorbing coatings based on AlSiOx□:W cermets, Sol. Energy. 150 (2017) 335–344.

Figure Captions

Fig. 1: (a)Transmittance (T), (b) Reflectance (R), (c) Refractive index (n) and (d) extinction coefficient (k) of $CrAlSiN_x$ and $CrAlSiO_yN_x$ as a function of wavelength (λ).

Fig. 2: XRD of the single layers. (S related to stainless steel structure.)

Fig. 3: SEM cross-section micrographs of (a) N-5Si and (b) ON-5Si samples.

Fig. 4: Schematic diagram of the simulated multilayer as obtained by SCOUT with simulated and experimental reflectance curves of the absorber design (a) D1 and (b) D2.

Fig. 5: Cross-sectional SEM images of samples D1 and D2.

Fig. 6: Reflectance of as deposited and after air and vacuum thermal annealed samples (the thermal emittance (ε) was calculated for 400 ºC).

Fig. 7: The spectra of RBS of the samples D1 and D2 as deposited and after air and vacuum annealing for 650 h.

Fig. 8: XRD diffractograms of as deposited samples D1 and D2 in the as deposited state and after air and vacuum annealing.

Fig. 9: Surface roughness imaged by AFM (5x5 μm^2) of sample D1: a) as deposited coating; b) after annealing at 600 ºC in vacuum and of sample D2: a) as deposited coating; b) after annealing at 600 ºC in vacuum.

Tables

Table I: D1 and D2 deposition parameters.

Sample	Layer	Target	Deposition time (min)	Reactive gas and partial pressure (Pa)	Thickness (nm)
D1	W	W	2:00	-	120
	$CrAlSiN_x$ (N-5Si)	CrAl+ 5 Si	1: 27	N_2 0.05	63
	$CrAlSiO_yN_x$ (ON-5Si)	CrAl+ 5 Si	0:23	N_2/O_2 (85%/15%) 0.07	16
	$SiAlO_x$	SiAl	1:29	O_2 0.06	77
D2	W	W	2:00	-	120
	$CrAlSiN_x$ (N-11Si)	CrAl+11 Si	2:20	N_2 0.05	59
	$CrAlSiO_yN_x$ (ON-11Si)	CrAl+11Si	1:26	N_2/O_2 (85%/15%) 0.07	35
	$SiAlO_x$	SiAl	1: 19	O_2 0.06	68

Table II: EDS chemical composition and thickness of N-11Si, ON-11Si, N-5Si and ON-5Si thick layers.

Layer	N at%	O at%	Al at%	Si at%	Cr at%	Si/(Si+Al+Cr)	N+O/(Al+Si+Cr)	(Al+Si)/Cr	Thickness (µm)
N-5Si	23	6	30	11	30	0.15	0.4	1.5	1.3
N-11Si	26	5	26	20	23	0.29	0.5	2.0	0.9
ON-5Si	27	18	25	8	22	0.145	0.8	1.5	1.4
ON-11Si	30	11	22	18	19	0.305	0.7	2.0	1.1